

See discussions, stats, and author profiles for this publication at:  
<https://www.researchgate.net/publication/222133898>

# Effects of interface wettability on microscale flow by molecular dynamics simulation. Int. J. Heat Mass Transfer

**Article** *in* International Journal of Heat and Mass Transfer · January 2004

Impact Factor: 2.38 · DOI: 10.1016/j.ijheatmasstransfer.2003.07.013

---

CITATIONS

123

---

READS

236

**2 authors:**



**Gyoko Nagayama**

Kyushu Institute of Technology

**31** PUBLICATIONS **370** CITATIONS

[SEE PROFILE](#)



**Ping Cheng**

Shanghai Jiao Tong University

**293** PUBLICATIONS **9,347** CITATIONS

[SEE PROFILE](#)

# Effects of interface wettability on microscale flow by molecular dynamics simulation

Gyoko Nagayama<sup>a</sup>, Ping Cheng<sup>b,\*</sup>

<sup>a</sup> *Department of Mechanical and Electrical Engineering, Tokuyama College of Technology, 3538 Takajo, Kume, Shunan, Yamaguchi 745-8585, Japan*

<sup>b</sup> *School of Mechanical and Power Engineering, Shanghai Jiaotong University, Shanghai 200030, China*

Received 17 July 2002; received in revised form 12 July 2003

## Abstract

Non-equilibrium molecular dynamic simulations have been carried out to study the effect of the interface wettability on the pressure driven flow of a Lennard–Jones (LJ) fluid in a nanochannel. The results show that the hydrodynamic boundary condition at the solid–liquid interface depends on both the interface wettability and the magnitude of the driving force. For a LJ fluid in a nanochannel with hydrophilic surfaces, the velocity profiles have the traditional parabolic shape. The no-slip boundary condition may break down when the driving force exceeds a critical value that overcomes the interfacial resistance. In such a case, the MD results show a pattern of an adsorbing layer sliding along the solid wall. For a LJ fluid in a nanochannel with hydrophobic interfaces, the results show that a gap exists between the liquid and the surface, resulting in almost frictionless resistance; the velocity shows a plug flow profile and the slip length is not constant but depends on the driving force. Furthermore, it is found that the non-uniform temperature and pressure profiles near the solid walls are owing to the effect of interface wettability.

© 2003 Elsevier Ltd. All rights reserved.

**Keywords:** Interface wettability; Pressure driven flow; Velocity slip; Interfacial resistance; Molecular dynamics simulation

## 1. Introduction

Simulation of microscale thermo-fluidic transport has attracted considerable attention in recent years owing to rapid advances in microelectronic fabrication technologies and the promise of emerging nano-technologies. For macroscopic flows, it has been well established that the boundary condition of a viscous fluid at a solid wall is one of “no-slip” condition in the continuum regime, while velocity slip at the wall occurs when the Knudsen number of the flow is greater than 0.001 [1]. The effect of the solid–liquid interface wettability on the boundary condition is negligible for flow in a macrochannel. However, the effect of the surface wettability on the interface boundary condition in mi-

croscale flows cannot be ignored since the molecular interaction at the interface may play an important role with the decrease of the domain size.

Recently, a number of papers [2–12] have appeared on the study of microscale flow at the solid–liquid interface to determine whether the traditional hydrodynamic boundary condition is valid. Tretheway and Menhart [2] performed an experiment and found that the apparent velocity slip existed in a microchannel coated with a hydrophobic monolayer while the no-slip boundary condition existed on a clean hydrophilic microchannel. Zhu and Granick [3] found experimentally that the no-slip boundary condition is satisfied only at low flow rates, and the magnitude of the velocity slip depends on the flow rate and the surface wettability. Based on molecular dynamics simulation, Barrat and Bocquet [6] obtained slip lengths of 30 molecular diameters on a surface with a contact angle of 140°, which is drastically different from the no-slip boundary

\* Corresponding author. Tel./fax: +86-21-6293-3107.

E-mail address: [pingcheng@sjtu.edu.cn](mailto:pingcheng@sjtu.edu.cn) (P. Cheng).

### Nomenclature

$D$	distance between two walls from the first solid layer
$D_z$	distance between two solid walls, which equals to $D - 2\sigma_1$
$F_x$	driving force
$k_B$	Boltzmann constant
$l_s$	length of slip
$M$	mass of a molecule
$N$	number of molecules
$P$	pressure
$r_{ij}$	distance between molecule $i$ and $j$
$T$	temperature
$U_c$	centerline velocity of the flow
$V$	volume of the bin
$V_{n,i}$	velocity component $i(=x, y, z)$ of molecule $n$
$\bar{V}_i$	mean velocity component $i(=x, y, z)$
$V_s$	slip velocity of the liquid adjacent to the wall

### Greek symbols

$\alpha$	potential energy factor to adjust the strength of hydrophilic interaction
$\beta$	potential energy factor to adjust the attraction for hydrophobic interaction
$\sigma$	length parameter of LJ potential
$\varepsilon$	energy parameter of LJ potential
$\delta$	thickness of interface region
$\theta$	contact angle
$\rho_l$	density of bulk liquid
$\rho_{\text{sat}}$	density of saturated liquid
$\phi$	potential energy

### Subscripts

l	liquid
s	solid

condition. Thompson and Troian [7] obtained both linear and non-linear responses of slip lengths for the Couette flow. Cieplak et al. [8] suggested that the slip length is related to the fluid organization near the solid wall and is independent of the type of flow. Most recently, experiments performed by Craig et al. [11] as well as by Zhu and Granick [12] show that the slip length is a function of the flow rate. These recent studies confirmed that both no-slip as well as slip velocity boundary condition may occur at the fluid/solid interface in microscale fluidic problems. In another paper, Wu and Cheng [13] found experimentally that interface wettability has noticeable effects on both pressure drop and convective heat transfer in microchannels. However, the mechanism of this effect from the microscale point of view has not yet been clarified.

The purpose of this paper is to examine the effect of surface wettability on pressure driven flows in order to better understand the fluidic flow behavior at a solid wall. We have carried out non-equilibrium molecular dynamic (NEMD) simulations of simple Lennard–Jones (LJ) fluids subject to an inlet driving force in a nanochannel. In the present work, multi-layers of platinum molecules are utilized to simulate the solid walls, and argon molecules are employed as a LJ fluid. A modified LJ potential function is used to represent different interface wettabilities by using different values of solid–liquid interaction parameters. The interfacial density profiles at different magnitudes of the driving force (in a steady non-equilibrium condition) and those without external force (in an equilibrium condition) are compared to clarify the characteristics of the solid–liquid interface structure. Also, the effects of the interface

wettability and the magnitude of the driving force on the velocity, temperature, and pressure profiles are discussed.

## 2. Simulation methods

In this paper, molecular dynamics simulations are performed for liquid molecules moving in a nanochannel bounded by two solid walls on the  $z$ -axis, subject to a driving force at the inlet as shown in Fig. 1. The simulation cell has the size of  $5.83 \times 3.85 \times 7.22 \text{ nm}^3$  and the distance separated between two walls is 5.41 nm. Each solid wall consists of four layers of molecules arranged as a FCC lattice and its  $\langle 111 \rangle$  surface is in contact with the liquid. For the sake of physical understanding, we assume that the solid walls are made of platinum and the LJ fluid is argon. For the geometry under consideration, there are 2688 platinum molecules corresponding to its density of  $21.45 \times 10^3 \text{ kg/m}^3$ . Initially the system is at 100 K, and, there are 2400 argon molecules (at its saturated liquid density) inside the nanochannel. Periodic boundary conditions with respect to the number of molecules are applied along the  $x$ - and  $y$ -directions. In the  $z$ -direction, outside each solid wall of the simulation cell, four layers of phantom solid molecules anchored by their lattice are located to model a semi-infinite potential field of the solid wall [14].

For the liquid–liquid interaction, the LJ potential is applied:

$$\phi(r_{ij}) = 4\varepsilon \left[ \left( \frac{\sigma}{r_{ij}} \right)^{12} - \left( \frac{\sigma}{r_{ij}} \right)^6 \right], \quad (1)$$

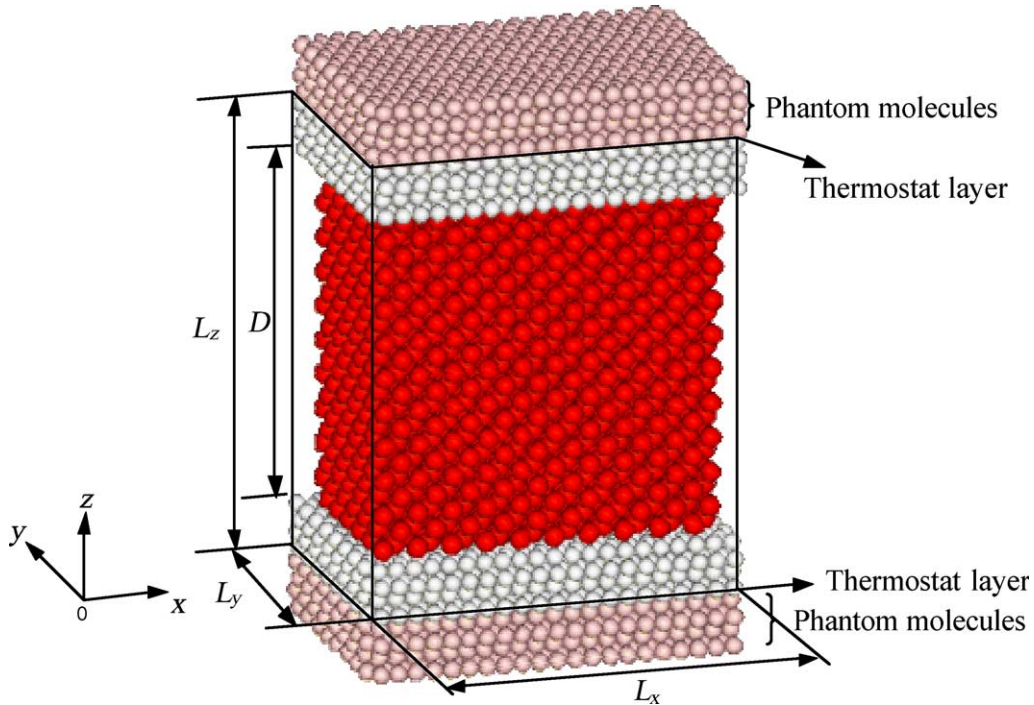


Fig. 1. Simulation system configuration of nanochannel with the size of  $L_x = 5.83$  nm ( $17\sigma_1$ ),  $L_y = 3.85$  nm ( $11\sigma_1$ ),  $L_z = 7.22$  nm ( $21\sigma_1$ ) and  $D = 5.41$  nm ( $16\sigma_1$ ). This configuration of the wall was prepared by four layers consisted by 1344 platinum molecules at each side. Only the outside layer of each wall is used to be a thermostat layer. Outside of the solid wall of the simulation system, phantom molecules anchored by their lattices are set to model a semi-infinite potential field of the wall.

where the length parameter  $\sigma = \sigma_1 = 3.405$  Å, and the energy parameter  $\varepsilon = \varepsilon_1 = 1.67 \times 10^{-21}$  J for argon. The LJ potential given by Eq. (1) is also applied for the solid–solid interaction with  $\sigma = \sigma_s = 2.475$  Å corresponding to the lattice constant 2.776 Å of platinum, and  $\varepsilon = \varepsilon_s = 8.35 \times 10^{-20}$  J ( $\approx 50\varepsilon_1$ ) for the potential well depth of Pt–Pt to model molecular vibration at the lattice. The method of tethering the solid molecules to a fixed lattice site [6] is not used in the present work.

For the solid–liquid interaction, the following modified LJ potential is used:

$$\begin{aligned} \phi_{sl}(r_{ij}) &= 4\varepsilon_{sl} \left[ \left( \frac{\sigma_{sl}}{r_{ij}} \right)^{12} - \beta \left( \frac{\sigma_{sl}}{r_{ij}} \right)^6 \right] \\ &= 4\alpha \sqrt{\varepsilon_1 \varepsilon_s} \cdot \left[ \left( \frac{\sigma_{sl}}{r_{ij}} \right)^{12} - \beta \left( \frac{\sigma_{sl}}{r_{ij}} \right)^6 \right], \end{aligned} \quad (2)$$

where  $\sigma_{sl} = (\sigma_1 + \sigma_s)/2$ , and the energy parameter  $\varepsilon_{sl}$  is given by  $\varepsilon_{sl} = \alpha \sqrt{\varepsilon_1 \varepsilon_s}$  based on the Lorentz–Berthelot combining rule [15,16]. Here,  $\alpha$  is the potential energy factor indicating the strength of hydrophilic interaction and  $\beta$  is the potential energy factor indicating the attraction for hydrophobic interaction. Eq. (2) is a modified form of the LJ potential, which is a combination of

the potential models used by Din and Michaelides [10] as well as by Barrat and Bocquet [6]. In this paper, the values of  $\alpha$  and  $\beta$  with responding values of the contact angle are taken from a recent paper [17] for the problem of droplet formation on a substrate. These values were used in simulation Cases (a)–(f) and are listed in Table 1. As shown from this table, Cases (a)–(c) at  $\beta = 1$  with zero contact angle are nanochannels with hydrophilic surfaces. As will be discussed in Section 3, the decreasing values of  $\alpha$  in Cases (a)–(c) representing decreasing strength of hydrophilic interactions. Thus, the values of  $\alpha = 1$ ,  $\alpha = 0.5$  and  $\alpha = \sqrt{\varepsilon_1/\varepsilon_s} = 0.14$  (i.e.,  $\varepsilon_{sl} = \varepsilon_1$ ) in Cases (a)–(c) represent strong, middle and weak hydrophilic interactions. Cases (d)–(f) at  $\alpha = 0.14$  and with decreasing values of  $\beta$ , having contact angles varying from approximately  $130^\circ$  to  $180^\circ$ , are hydrophobic surfaces. Thus, the values of  $\beta = 0.5$ ,  $\beta = 0.3$  and  $\beta = 0.1$  in Cases (d)–(f) represent weak, middle and strong hydrophobic interactions respectively.

All simulations were performed with a time step of 5 fs and a selected cut off radius of  $3.5 \sigma_1$  for the spherically truncated and shifted potential. The equations of motion were integrated by the Velocity Verlet algorithm. After achieving a steady state from the initial state, the equilibrium system (without thermostat and external

Table 1  
Simulation cases and the values of  $\alpha$  and  $\beta$  used in Eq. (2)

Simulation cases	$\alpha$	$\beta$	$\theta$ [°]	$\delta$ [nm]	$\bar{\rho}/\rho_{\text{sat}}^a$	$\rho_{\text{max}}/\rho_{\text{sat}}^a$	$\Delta\rho = \rho_l - \rho_{\text{sat}}$ [kg/m <sup>3</sup> ]
(a)	1	1	0	2.061	1.039	4.174	−0.195
(b)	0.5	1	0	1.959	1.037	3.699	−0.096
(c)	0.14	1	0	1.790	1.012	3.267	−0.024
(d)	0.14	0.5	130 ± 7	1.385	0.968	2.242	0.048
(e)	0.14	0.3	160 ± 8	1.216	0.945	1.526	0.062
(f)	0.14	0.1	180	1.216	0.932	1.528	0.076

The contact angle  $\theta$  are taken from Ref. [17]. The thickness of interface region  $\delta$ , the mean and maximum density of interface region  $\bar{\rho}$  and  $\rho_{\text{max}}$ , the density difference between the bulk liquid and the saturated liquid  $\Delta\rho = \rho_l - \rho_{\text{sat}}$  are obtained from equilibrium simulations.

<sup>a</sup>  $\rho_{\text{sat}} = 1311.2 \text{ kg/m}^3$  for  $T = 100 \text{ K}$ .

force) at 100 K was simulated. Then, the NEMD simulation with external force and thermostat was carried out from this equilibrium state.

In earlier MD work on Poiseuille flow [6,8,9], external force was applied uniformly to each liquid molecule similar to that of a gravity-driven flow. Under such a situation, a large amount of energy was added to the system by the external force, and temperature control was applied to all wall molecules [9] or fluid molecules [6,8]. In order to obtain more realistic results for a pressure driven flow in the present work, the external force was applied only at the inlet region of the channel to drive the flow. The length of the inlet region is defined as one molecular diameter of argon ( $\sigma_l = 3.405 \text{ \AA}$ ), which is about 4.7% of the channel length. Because an external driving force is applied and energy has been added to the system that may lead to the generation of heat, the simple velocity scaling technique [18] is applied only to the outside layer of each wall (not all wall atoms) to maintain a constant wall temperature there. This would allow the possibility of a temperature slip at the interface. Similarly, a constant inlet temperature of 100 K (the same as the wall) was applied by velocity scaling to the liquid molecules in the inlet region, which is about 5% of the total number of liquid molecules. It should be noted that no thermostat was coupled to the liquid or solid molecules elsewhere for all simulation cases.

### 3. Results and discussion

If there is no wall effect, the channel would be filled with 2400 molecules to achieve the saturated density of liquid argon at 100 K with  $\rho_{\text{sat}} = 1311.2 \text{ kg/m}^3$ . Therefore, the following results obtained based on 2400 liquid molecules are for the flow near the saturated state. In all NEMD simulations, 2.5 ns were used for the data sampling, and the local data of the velocity, temperature and pressure were collected by  $8 \times 8$  bins in the  $x$ - and  $z$ -directions. The segmental width of each bin

was set to be  $7.29 \text{ \AA}$  in the  $x$ -direction and  $6.76 \text{ \AA}$  in the  $z$ -direction.

#### 3.1. Interface structure

We now examine the effect of interface wettability on the interface structure by comparing the density profiles near the liquid/solid interfaces for the equilibrium and non-equilibrium conditions. To obtain the interface density distribution, narrow divisions of 80 bins in the  $z$ -direction were used and the segmental width of each bin was set at  $0.676 \text{ \AA}$  ( $\approx \sigma_l/5$ ).

Fig. 2 shows typical snapshots of the simulation systems and the density profiles of liquid argon in the equilibrium condition in which no external force and no thermostat were applied. The shadows in the right-hand side's figures illustrate the solid walls and the vertical dashed lines show the position of the molecular mass center of the first solid layer. Results for the hydrophilic surface (a) with  $\alpha = 1$  and  $\beta = 1$  are presented in Fig. 2(a). It is shown that the liquid molecules in the snapshots distribute orderly in the vicinity of the solid interface due to strong solid–liquid interactions. This interface structure (i.e., the solid-like structure formed by the adsorption layers of argon molecules) and its oscillatory characteristics of the density profiles are in agreement with most of earlier studies [19,20]. It should be noted that the oscillatory characteristics of density profiles in this interface structure are owing to the fact that the molecules are orderly distributed adjacent to the walls and the width of the bin was chosen to be smaller than the molecular diameter. Due to the nanoscale of the separate distance of the walls, the effect of wall adsorption on the bulk density of the liquid is very prominent. Thus, the density of the bulk liquid has a lower value than its saturated value of  $\rho_{\text{sat}} = 1311.2 \text{ kg/m}^3$ . The interface region, defined as the region where its local density deviates from its bulk value, is characterized by its thickness  $\delta$  which is typically several molecular diameters as listed in Table 1. It is shown that the



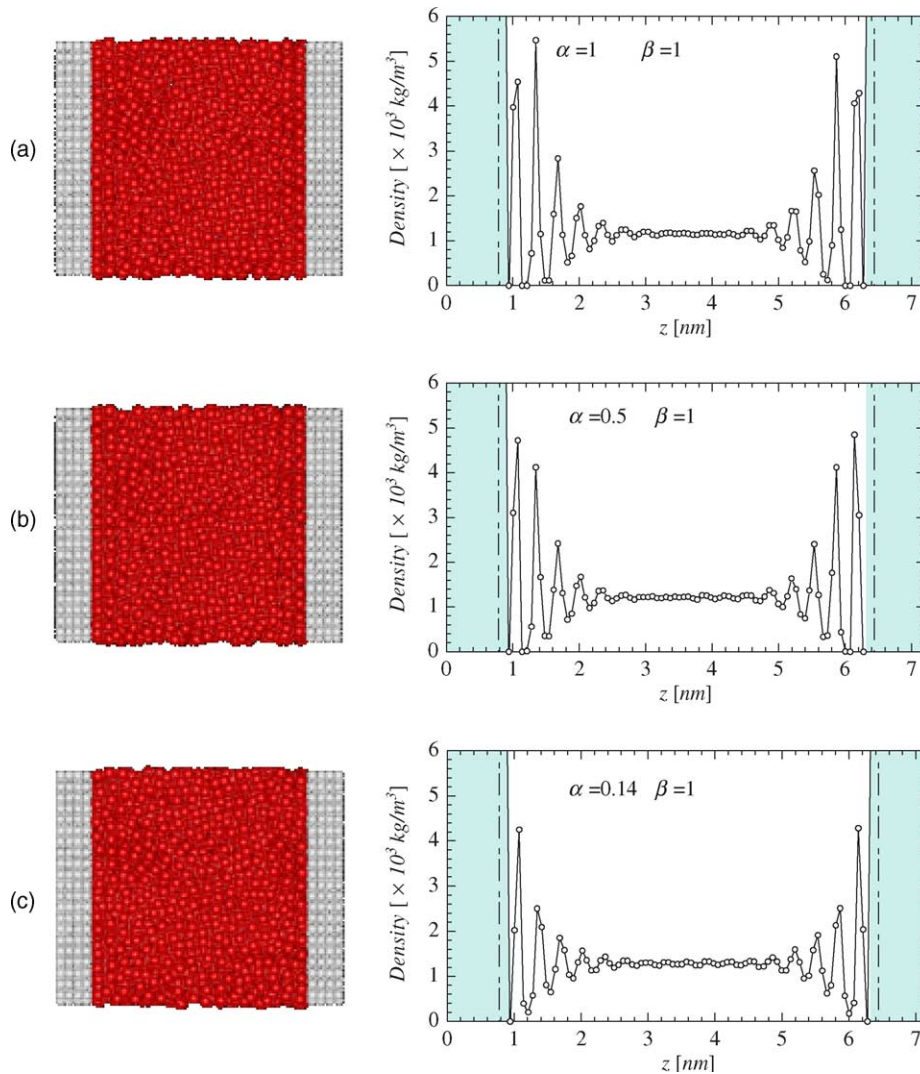


Fig. 2. Snapshots and particular description of density distribution in equilibrium states of 100 K. The solid line is a guide for the eye.

thickness of the interface region decreases with the decreasing of  $\alpha$ , implying the hydrophilic interaction has decreasing strengths. For Case (a), the thickness is about 2.061 nm ( $\approx 6\sigma_l$ ) with three orderly molecular layers adjacent to each wall. Figs. 2(b) and (c) show the results of a hydrophilic interface ( $\beta = 1$ ) with middle ( $\alpha = 0.5$ ) and weak ( $\alpha = 0.14$ ) solid–liquid interactions. The solid-like layers near the walls can also be found in these two cases, although the thickness of the interface region becomes thinner. Figs. 2(d)–(f) show the results for hydrophobic cases ( $\beta = 0.5, 0.3, 0.1$ ) corresponding to the partial wetting and non-wetting surfaces. It is shown that the molecules adjacent to the solid walls were more randomly distributed comparing with those in Figs. 2(a)–(c). Consequently, the density variation in the interface regions became smaller and smaller. As the at-

traction of the modified LJ potential in Eq. (2) was weakened by reducing  $\beta$ , the interfacial layer structure was less obvious and the bulk liquid results in a super-saturated situation. In cases of Figs. 2(e) (with  $\beta = 0.3$ ) and (f) (with  $\beta = 0.1$ ), a gap (with density equal to zero) is formed between the liquid and the walls, which drastically differ from the hydrophilic interface. In Ref. [21], the existence of a gap between liquid and solid formed by entrained or soluble gas in the flowing liquid has been suggested to increase the velocity slip. The present MD results thus support this speculation. Table 1 lists the ratios of the mean ( $\bar{\rho}$ ) and the maximum density of interface region ( $\rho_{\max}$ ) to the saturated value ( $\rho_{\text{sat}} = 1311.2 \text{ kg/m}^3$ ) for the six simulated cases. The mean density of the layers near the wall is higher than the value of the bulk liquid for the hydrophilic cases,

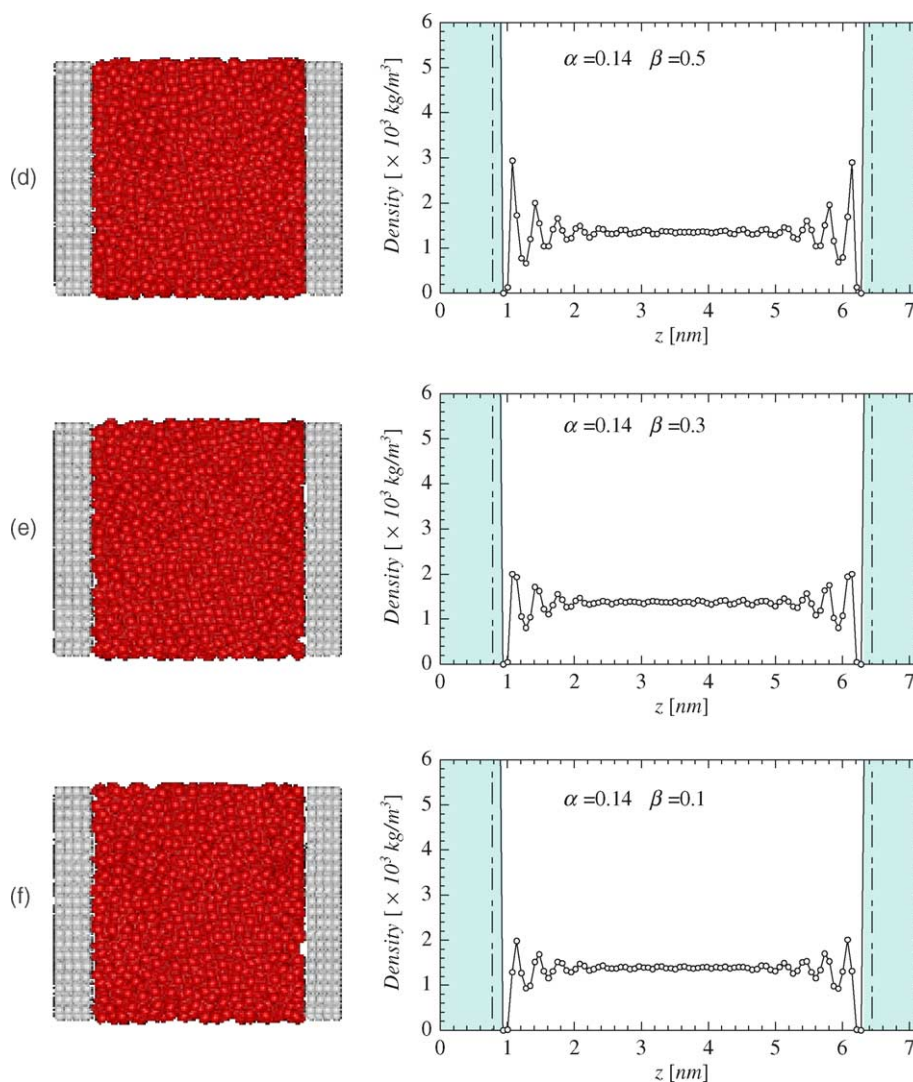


Fig. 2 (continued)

while it is lower for the hydrophobic cases. The differences between saturated density ( $\rho_{\text{sat}}$ ) and the bulk liquid density are also presented in Table 1. It is shown that the bulk liquid results in the subsaturated situation for the hydrophilic surface, while the supersaturated situation is caused by the hydrophobic surface.

Fig. 3 shows the effect of external force on the density profiles based on the NEMD simulation where only half of the nanochannel is shown. Again, the shadows illustrate the solid walls and the dashed lines show the position of the molecular mass center of the first solid layer. Simulations were carried out with four different external forces of  $1.96 \times 10^{-1}$  pN (square), 1.96 pN (diamond), 7.55 pN (triangle/up) and 9.80 pN (triangle/down) at the inlet, corresponding to the inlet driving pressures of 1.32, 13.19, 50.76 and 65.93 MPa respec-

tively. The solid line is the density profile of equilibrium simulation without inlet driving force (i.e., the results of Fig. 1). It is shown that there is no significant deviation from the equilibrium interface structure while the thickness of the interface region is almost independent of the driving force. Thus, the driving force has no significant influence on the interface structure of the density profile. Simulations were also carried out with a very large driving force corresponding to the inlet pressure of 130 MPa for Case (a), which resulted in slight decreases in the thickness of interface region and a slight increase in the density of the first adsorption layer. However, such a high driving force could not be achieved in reality in a laboratory. Therefore, we can conclude that the interfacial density structure is independent of the magnitude of the driving force, and is a characteristic de-

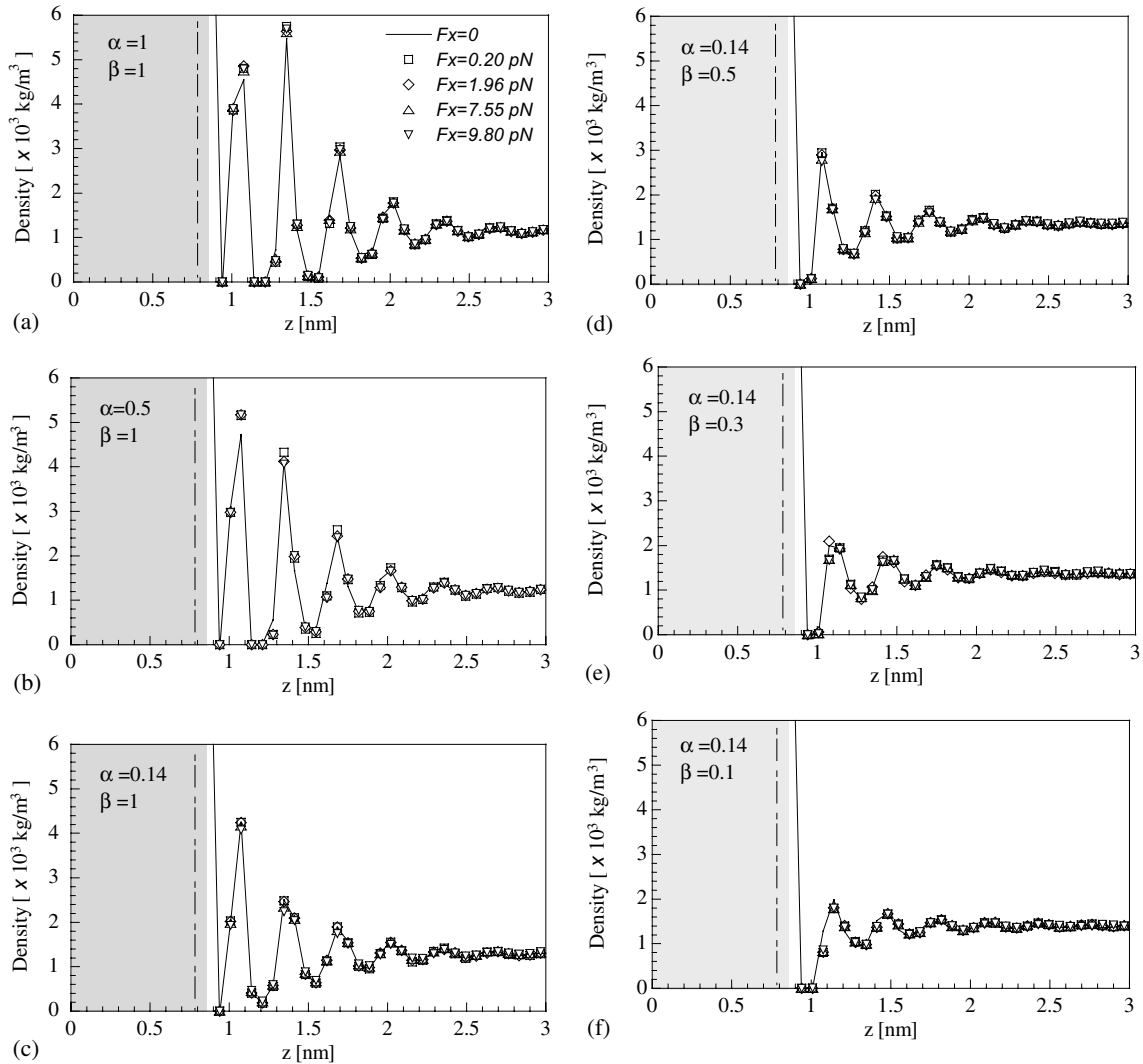


Fig. 3. Interfacial structure and the driving force with different interfacial wettability.

terminated only by the interface wettability for the confined liquid flow near the saturated state.

### 3.2. Velocity profile

Fig. 4 illustrates velocity profiles of the flow in the  $z$ -direction along the nanochannel. Depending on the surface wettability, it is shown that the velocity profiles can have either a parabolic shape or a plug flow shape. With the same surface wettability condition, the velocity profiles have a similar shape under different driving forces. For hydrophilic surfaces of Cases (a)–(c), the velocity profiles are similar to the macroscopic flow of parabolic shape and the mean velocity of the flow increases with increasing driving force. Comparing Case (a) with Cases of (b) and (c), it appears that the stronger

interfacial interaction (with higher value of  $\alpha$ ) causes higher viscosity at the interface region. As seen from this figure, no-slip boundary condition still holds at the well-wetted surface (a) for the driving force presenting, and the velocity gradient takes place inside the liquid. However, at the interface (b), although no-slip is satisfied for the low driving force, it obviously breaks down when the driving force is increased to 7.55 pN (triangle) and 9.80 pN (circle). Similar situation is found for Case (c) where the apparent slip occurs when the driving force is larger than 1.96 pN (diamond). This implies that Case (c) has a less interfacial resistance than that of Cases (b) and (a), and the velocity slip occurs at the interface when the driving force overcomes the interfacial resistance. On the other hand, simulation results for hydrophobic surfaces of Cases (d), (e) and (f) show a plug flow profile



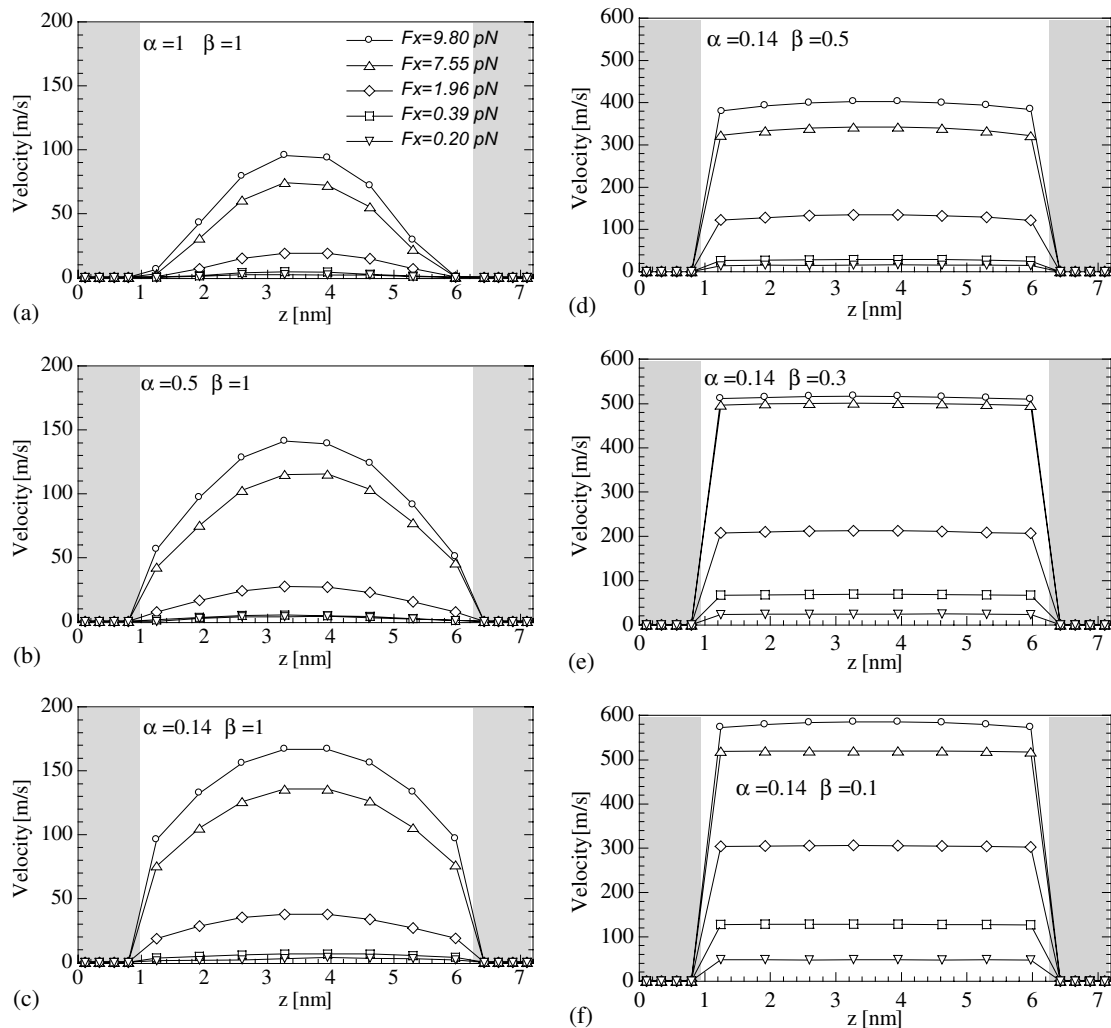


Fig. 4. Velocity profiles in the  $z$ -direction of the pressure driven flow with different interface wettability. The solid line is a guide for the eye.

with apparent velocity slip at the wall even at low driving forces. Away from the walls, the flat velocity profiles are in parallel with each other under different driving forces.

Fig. 5 shows the velocity distribution in the streamwise direction ( $x$ -direction) for Cases (a)–(f) under the same driving force of 1.96 pN. It is shown that the streamwise velocity is almost constant along the channel direction. It is seen from this figure that the mean velocity of the flow in hydrophilic channels is lower than those in hydrophobic channels for the same value of the driving force. This implies that hydrophobic surfaces have a smaller interfacial hydrodynamic resistance than hydrophilic surfaces. Thus, a smaller driving force is required for flows in microchannels if interface wettability is reduced.

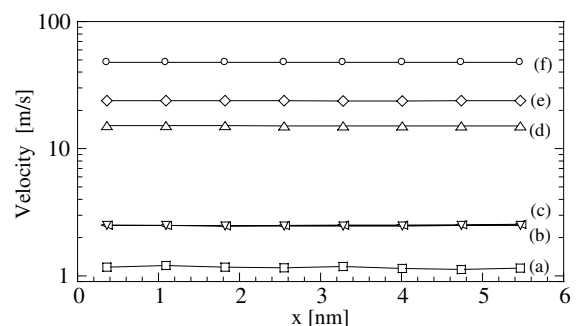
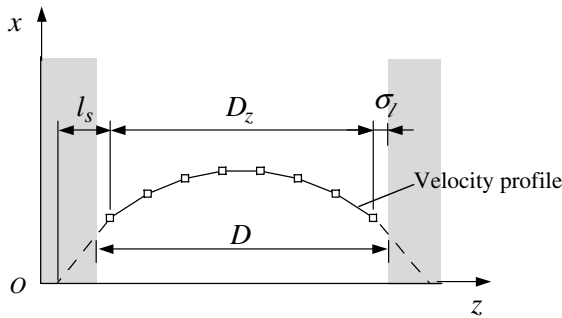


Fig. 5. Velocity profiles in the  $x$ -direction of the pressure driven flow with different interface wettability. The solid line is a guide for the eye.

Fig. 6. Definition of the length of slip  $l_s$ .

### 3.3. Interfacial velocity slip

As shown in Fig. 6 we can obtain the slip length  $l_s$  by extrapolating the velocity profile from the position in the fluid (with one atomic distance from the first solid layer) to where the velocity would vanish within the solid. It should be note that the slip length  $l_s$ , as defined here, is not the same as those defined according to the Navier boundary condition [22] (see Appendix A). When the boundary condition of vanishing velocity occurring at  $l_s + D_z/2$  from the centerline of the channel is applied to the Stokes flow between two infinite parallel plates, the solution for the slip velocity  $V_s$  near the wall normalized by the centerline velocity  $U_c$  is

$$\frac{V_s}{U_c} = 1 - \left(1 + \frac{2l_s}{D_z}\right)^{-2}, \quad (3)$$

where  $D_z$  is the distance shown in Fig. 6. Eq. (3) gives the no-slip boundary condition when  $l_s = 0$  or when  $D_z$  is much larger than  $l_s$  as in most of the macroscopic phenomena. If  $l_s$  is finite, the importance of the term  $2l_s/D_z$  in Eq. (3) increases as  $D_z$  is decreased. Therefore, if  $D_z$  is at the micro- and nano-length scales, the slip velocity may be significant even if the slip length  $l_s$  is still in nano-length scales. For example, in the case when the ratio  $2l_s/D_z$  is close to 1, Eq. (3) gives the slip velocity being 75% of the centerline velocity. Eq. (3) also shows

that the constant slip length will result in the constant normalized slip velocity.

Table 2 summarizes the results of the slip length  $l_s$  for surfaces (a)–(e) by fitting the velocity profiles. It is shown that for a given surface with fixed wettability, the slip length is a function of the driving force and is not a constant. Although the variation of the slip length is small for a hydrophilic surface, it shows an upward trend with increasing inlet driving force. For a hydrophobic surface, the slip length increases dramatically with increasing driving force. Thus, the present MD results agree with experimental data that the slip length is a function of the flow rate [3,11,12].

Fig. 7 is a comparison of the velocity slip given by Eq. (3) with the MD results. As mentioned earlier, the slip velocity is defined to be the velocity sampled in the first bin near the wall, where its center is one atomic distance from the solid wall. Fig. 7(a) illustrates the variation of the slip velocity as a function of the inlet driving force. The slip velocity increases with increasing inlet driving force, and a large magnitude of velocity slip is observed at the non-wetting interface (with  $\alpha = 0.14$  and  $\beta = 0.1$ ). Also, by substituting the results of the slip length listed in Table 2 into Eq. (3), the normalized slip velocity is obtained. Fig. 7(b) presents the normalized slip velocity where the dashed lines are the results estimated by Eq. (3) and the MD results represented by symbols. It is shown that the slip velocity at a hydrophobic interface is more than 90% of the centerline velocity, while it is less than 50% of the centerline velocity at a hydrophilic surface. For surface (a) with  $\alpha = 1$  and  $\beta = 1$ , although no-slip boundary condition is valid for various inlet driving forces presented in Fig. 4(a), this boundary condition is not valid when an extremely large driving force is applied. For the latter case, results show that the liquid molecules near the wall sliding along the solid wall, and the velocity of the adsorption layer adjacent to the wall can reach 40% of the centerline velocity for the parameters chosen. Simulation results presented in Fig. 7(b) shows that the normalized slip velocity is not constant but is a function of the inlet driving force.

Table 2  
Variation of the slip length  $l_s$  as a function of the inlet driving force  $F_x$

Case	$F_x$ [pN] (per molecule)					
$l_s$ [nm]	0.10	0.20	0.39	1.96	7.55	9.80
(a)	0	0	0.03	0.04	0.06	0.07
(b)	0	0.31	0.41	0.60	0.93	0.94
(c)	0	1.22	1.44	1.47	1.71	1.74
(d)	11.13	11.38	14.63	14.63	27.63	29.13
(e)	21.75	24.62	39.43	57.09	118.65	137.95

Simulation cases (a)–(e) are corresponding to the different interfacial wettability with detailed parameters shown in Table 1.

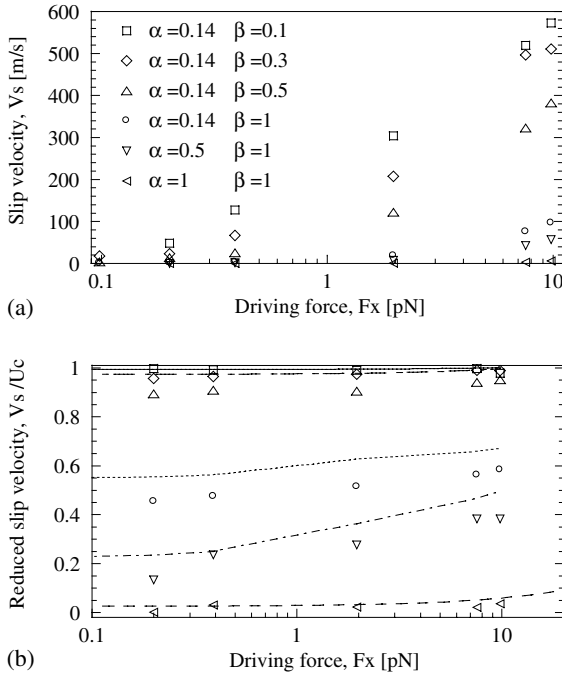


Fig. 7. Variation of the slip velocity as a function of the inlet driving pressure. Dashed lines are results estimated by Navier's equation (3) with substituting the non-constant length of slip shown in Table 2 (from top: (e)–(a)).

### 3.4. Temperature profiles

The local temperature  $T$  of each bin can be obtained from

$$T = \frac{1}{N} \sum_{n=1}^N \frac{2}{3k_B} \sum_{i=1}^3 \frac{1}{2} m (v_{n,i} - \bar{v}_i)^2, \quad (4)$$

where  $N$  is the molecular number in the bin,  $k_B$  is the Boltzmann constant,  $m$  is the mass of the liquid molecule,  $v_{n,i}$  is the velocity of molecule  $n$  in the  $i$  ( $=x, y, z$ ) direction, and  $\bar{v}_i$  is the mean velocity of the macroflow in the bin.

The temperature profiles shown in Fig. 8 are time-averaged data sampled during 2.5 ns. In order to obtain realistic temperature distribution, no thermostat was coupled directly to the liquid molecules (except the inlet region) and temperature control was only performed to the outside solid layers of the nanochannel. For the hydrophilic surface (a), it is found that constant temperature distribution in the liquid between the walls of the nanochannel, which is consistent with the no-slip boundary condition. The heat generated by the internal friction of the liquid is transferred to solid molecules and is then removed by the thermostat. For hydrophilic surfaces (b) and (c), similar thermal behavior is observed for a small driving force. However, for large driving forces that lead to the apparent velocity slip at the

boundary layer, the temperature distribution in the liquid between the walls of the nanochannel has a M shape: there is a temperature peak near the solid wall although the temperature at the center of the channel remained at the wall temperature of 100 K. Since increasing the inlet driving force results in a significant increase in the relative velocity between liquid and solid molecules, heat is generated by the interfacial friction between liquid and solid molecules. Thus, the local temperature near the solid–liquid interface is increased and a temperature slip occurs at the interface. Similar situation is found for the hydrophobic surfaces (d) and (e). Because the interface resistance decreases with reducing the surface wettability, the temperature peak shows a lower value in Case (e) even if the surface (e) has a larger slip velocity. Similarly, for the surface (f) where the interfacial resistance is supposed to be the lowest of all cases, the interfacial friction shows less effect on the temperature profile. This indicates that the interfacial friction plays an important role on the temperature distribution between the walls in the microchannel.

### 3.5. Pressure profiles

According to the virial theorem, the local pressure  $P$  of each bin is

$$P = \frac{Nk_B T}{V} - \frac{1}{6V} \sum_{i=1} \sum_{j>1} r_{ij} \frac{d_\phi(r_{ij})}{dr_{ij}}, \quad (5)$$

where  $V$  is the volume of the bin. The first term in the right side is for the momentum flux caused by the molecular motion while the second term is for the contribution of the intermolecular forces. Long-range corrections were applied for the calculation of the pressure [23].

Fig. 9 shows the time average pressure profiles of liquid argon in the nanochannel for Cases (a), (c) and (d). It appears that the liquid pressure in the center of the nanochannel decreases when the driving force is increased. For the hydrophilic surface (a), it is shown that the pressure distribution is not uniform in the  $z$ -direction and there are two low pressure zones in the adsorption layers adjacent to the walls. Since the interfacial interaction results in the strong attraction force in the adsorption layer, the low values are the result of disjoining pressure at the solid–liquid interface. For hydrophilic surfaces (b) and (c), the pressure variation at the interface is small for low driving forces, while a uniform distribution is found with increasing driving force. However, for hydrophobic surfaces, the pressure near the solid wall is higher than the bulk value due to the repulsive interaction between liquid and solid molecules. Since the pressure profiles of Cases (e) and (f) are similar to that of Case (d), we only show the results of Case (d) in Fig. 9.

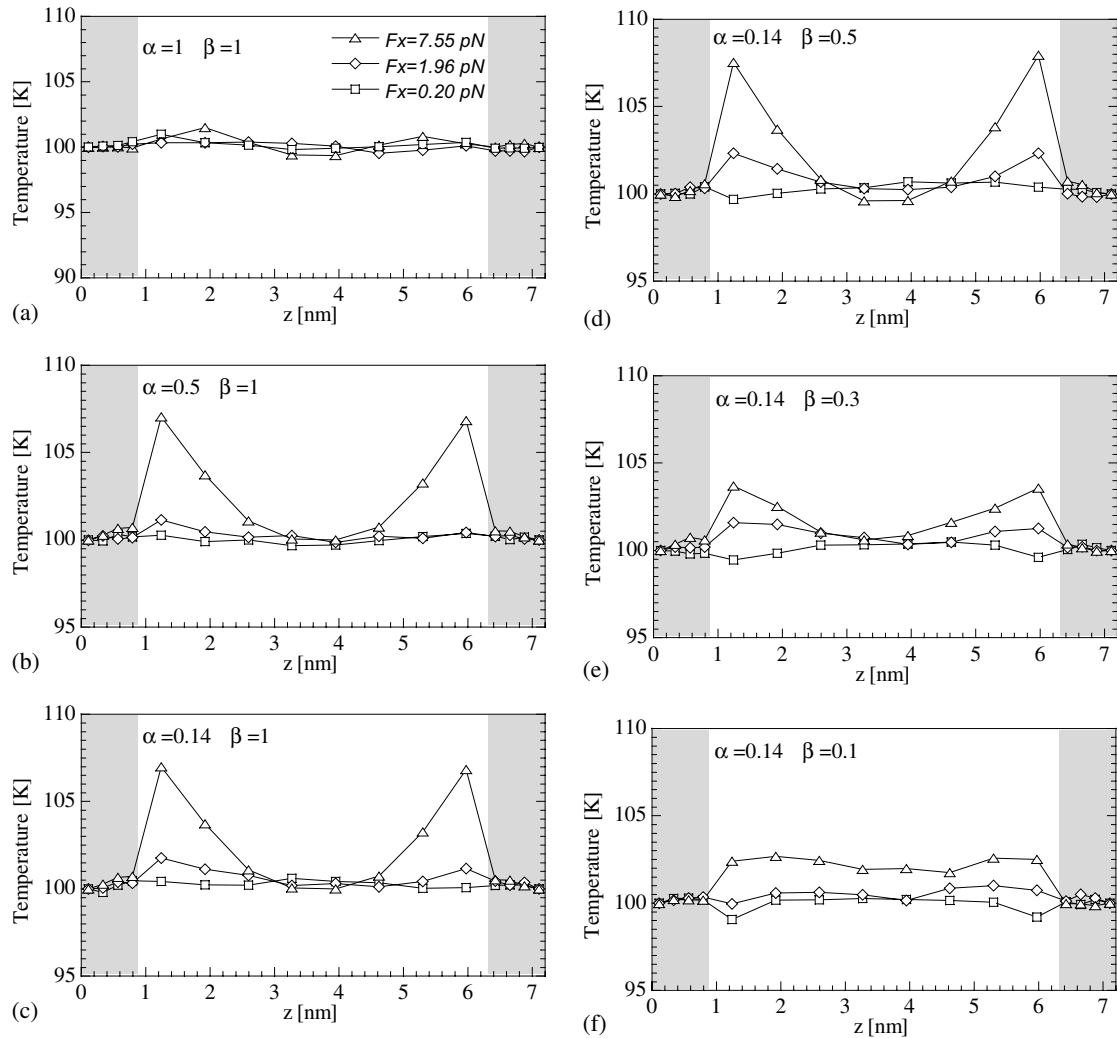


Fig. 8. Temperature profiles of the pressure driven flow with different interface wettability. The solid line is a guide for the eye.

#### 4. Conclusions

The pressure driven flow of a LJ fluid is investigated based on the molecular dynamics simulation in this paper. The following conclusions may be drawn from the present study:

1. The effect of surface wettability is important in determining interfacial hydrodynamic resistance. A hydrophobic surface has lower interfacial resistance than a hydrophilic interface, which supports the experimental data [13]. Also, the interface structure is independent of the driving force.
2. Solid–liquid interface boundary condition of the microscale flow depends on both the interfacial resistance (surface wettability) and the external driving force. The velocity slip at the hydrophilic interface

is the result of the driving force overcoming interfacial resistance, while interfacial friction of the hydrophobic surface is reduced because a gap exists between the liquid and the wall.

3. The velocity profile in a nanochannel with hydrophilic surface is of parabolic shape while that with hydrophobic surface is of plug flow shape. As far as the authors are aware, no previous paper has reported that the velocity profile in a microchannel with hydrophobic surfaces is of the shape of a plug flow.
4. The temperature and pressure profiles are distributed non-uniformly in the direction perpendicular to the channel due to the effect of interface wettability. The temperature of the liquid near the interface region increases when the interfacial friction is increased. This implies that the viscous dissipation effect is important in microscale fluidic flows. The

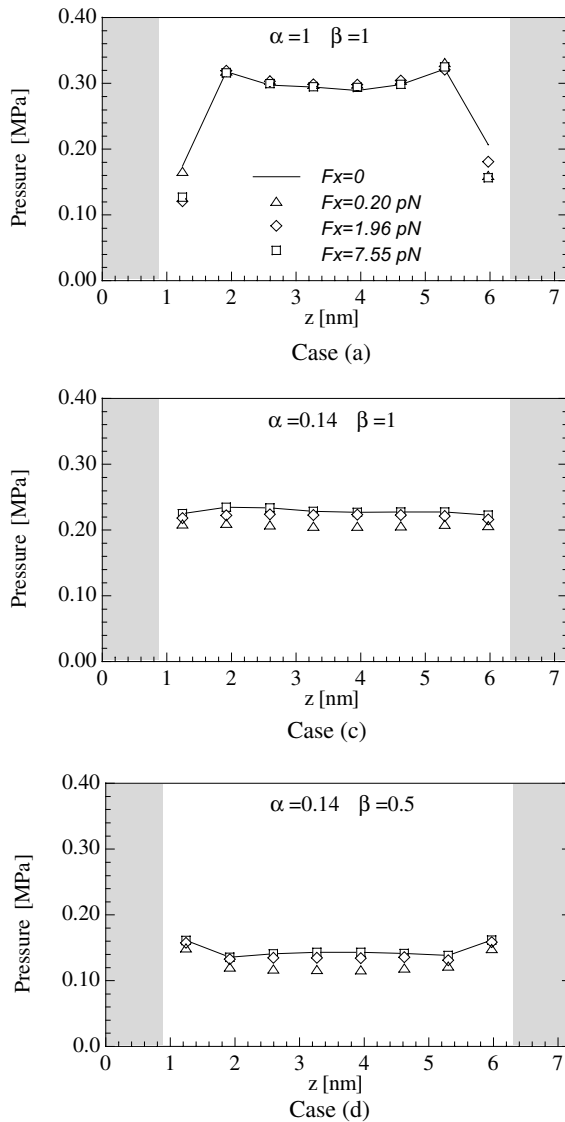


Fig. 9. Pressure profiles of the pressure driven flow with different interface wettability. The solid line is a guide for the eye.

M shape temperature profiles of the liquid in micro-channel flow has not been found in previous MD simulations.

#### Appendix A. The slip length based on linear Navier boundary

The linear Navier boundary condition [22] defines the slip length  $l_s$  as  $l_s = V_s/\dot{\gamma}$ , where  $\dot{\gamma}$  is the shear rate, which equals  $dV_s/dz$ . When the linear Navier boundary condition is applied to the Stokes flow between two infinite

parallel plates, the solution for the slip velocity  $V_s$  near the wall normalized by the centerline velocity  $U_c$  is

$$\frac{V_s}{U_c} = \left(1 + \frac{D_z}{4l_s}\right)^{-1}. \quad (\text{A.1})$$

#### References

- [1] M. Gad-el-Hak, The fluid mechanics of microdevices—The Freeman Scholar lecture, *J. Fluid Eng.* 121 (1999) 5–32.
- [2] D.C. Tretheway, C.D. Menhart, Apparent fluid slip at hydrophobic microchannel walls, *Phys. Fluids* 14 (3) (2001) L9.
- [3] Y. Zhu, S. Granick, Rate-dependent slip of Newtonian liquid at smooth surfaces, *Phys. Rev. Lett.* 87 (2001) 096105.
- [4] K. Watanabe, Yanuar, H. Udagawa, Drag reduction of Newtonian fluid in a circular pipe with a highly water-repellant wall, *J. Fluid Mech.* 381 (1999) 225–238.
- [5] M. Hasegawa, A. Yabe, S. Matsumoto, H. Nariai, Drag reduction and thermal behavior of nanoscale concave-convex surfaces, *Therm. Sci. Eng.* 7 (6) (1999) 133–138.
- [6] J. Barrat, L. Bocquet, Large slip effect at a nonwetting fluid–solid interface, *Phys. Rev. Lett.* 82 (23) (1999) 4671–4674.
- [7] P.A. Thompson, S.M. Troian, A general boundary condition for liquid flow at solid surfaces, *Nature* 389 (1997) 360–362.
- [8] M. Cieplak, J. Koplik, J.R. Banavar, Boundary conditions at a fluid–solid interface, *Phys. Rev. Lett.* 86 (5) (2001) 803–806.
- [9] K.P. Travis, K.E. Gubbins, Poiseuille flow of Lennard–Jones fluids in narrow slit pores, *J. Chem. Phys.* 112 (4) (2000) 1984–1994.
- [10] X.D. Ding, E.E. Michaelides, Kinetic theory and molecular dynamics simulations of microscopic flows, *Phys. Fluids* 9 (12) (1997) 3915–3925.
- [11] V.S.J. Craig, C. Neto, D.R.M. Williams, Shear-dependent boundary slip in an aqueous Newtonian liquid, *Phys. Rev. Lett.* 87 (5) (2001) 054504.
- [12] Y.X. Zhu, S. Granick, Apparent slip of Newtonian fluids past adsorbed polymer layers, *Macromolecules* 35 (2002) 4658–4663.
- [13] H.Y. Wu, P. Cheng, An experimental study of convective heat transfer in silicon microchannels with different surface conditions, *Int. J. Heat Mass Transfer* 46 (2003) 2547–2556.
- [14] S. Maruyama, T. Kimura, A study on thermal resistance over a solid–liquid interface by the molecular dynamics method, *Therm. Sci. Eng.* 7 (1) (1999) 63–68.
- [15] E.M. Yezdimer, A.A. Chialvo, P.T. Cummings, Examination of chain length effects on the solubility of alkanes in near-critical and supercritical aqueous solutions, *J. Phys. Chem. B* 105 (2001) 841–847.
- [16] Delhommelle, P. Millie, Inadequacy of the Lorentz–Berthelot combining rules for accurate predictions of equi-

- librium properties by molecular simulation, *Mol. Phys.* 99 (8) (2001) 619–625.
- [17] G. Nagayama, P. Cheng, A molecular dynamics study on the interface wettability of a LJ droplet on a platinum substrate, in preparation.
- [18] R.J. Sadus, *Molecular Simulation of Fluids*, first ed., Elsevier, Netherlands, 1999, pp. 305–307.
- [19] S. Somers, H.T. Davis, Microscopic dynamics of fluids confined between smooth and atomically structured solid surface, *J. Chem. Phys.* 96 (7) (1992) 5389–5407.
- [20] I. Bitsanis, J.J. Magda, M. Tirrell, H.T. Davis, Molecular dynamics of flow in microscopes, *J. Chem. Phys.* 87 (3) (1987) 1733–1750.
- [21] E. Ruckenstein, P. Rajora, [On the no-slip boundary condition of hydrodynamics](#), *J. Coll. Interf. Sci.* 96 (1983) 488.
- [22] S. Glodstein, in: *Modern Developments in Fluid Dynamics*, vol. 2, Dover, New York, 1965, p. 676.
- [23] [M.P. Allen, D.J. Tildesley, Computer Simulation of Liquids](#), Clarendon Press, Oxford, 1989, pp. 64–65.